Journal of Hazardous Materials 178 (2010) 427–433

Contents lists available at ScienceDirect

Journal of Hazardous Materials

journal homepage: www.elsevier.com/locate/jhazmat

Preparation of ordered mesoporous Ag/WO_3 and its highly efficient degradation of acetaldehyde under visible-light irradiation

Songmei Sun, Wenzhong Wang*, Shaozhong Zeng, Meng Shang, Ling Zhang

State Key Laboratory of High Performance Ceramics and Superfine Microstructure, Shanghai Institute of Ceramics, Chinese Academy of Sciences (SICCAS), No. 1295 Dingxi Road, Shanghai 200050, PR China

ARTICLE INFO

Article history:
Received 17 November 2009
Received in revised form 17 January 2010
Accepted 19 January 2010
Available online 25 January 2010

Keywords:
Photocatalyst
Tungsten trioxide
Silver loaded
Mesoporous structure

ABSTRACT

A highly active photocatalyst, silver loaded mesoporous WO_3, was successfully synthesized by an ultrasound assisted insertion method. The photodegradation of a common air pollutant acetaldehyde was adopted to evaluate the photocatalytic performance of the as-prepared sample under visible-light irradiation. The photocatalytic activity was about three and six times higher than that of pure mesoporous WO_3 and nitrogen-doped TiO_2, respectively. The photocatalytic mechanism was investigated to understand the much enhanced photocatalytic activity, which was mainly attributed to the largely improved electron–hole separation in the Ag–WO_3 heterojunction.

1. Introduction

In recent years, numerous studies have been reported on semiconductor photocatalysis which can utilize solar energy to decompose harmful organic pollutants in air and aqueous systems [1–5]. Among the semiconductors employed, TiO_2 is the most extensively studied photocatalyst because of its low cost, high efficiency and stability. However, TiO_2 is only active in the ultraviolet (UV) light range due to its wide band gap. To obtain visible-light-driven photocatalysts so as to utilize visible light, doping or ion-implanting has been used to modify TiO_2 [6–9], but dopants usually act as recombination centers between the photogenerated electrons and holes, which greatly reduced the photocatalytic activities [10]. Thus researchers are devoted in searching for other candidates to solve this problem.

Tungsten trioxide (WO_3), which possesses a small band gap of 2.4–2.8 eV, has many advantages for visible-light-driven photocatalysis such as strong adsorption within the solar spectrum, stable physicochemical properties, and resilience to photocorrosion effects [11–14]. In addition to the visible-light absorption, there are many other factors influencing the photocatalytic activity, such as the potential levels of energy bands, the separations of photogenerated electron–hole pairs and the microstructures of photocatalysts, *etc*. Like other simple binary metal oxides, WO_3 has a deep valence band which is mainly composed of O 2p orbitals. The deep valence band combined with the small band gap results in a low conduction band level, which limits the photocatalysts to react with electron acceptors [15–17] and then increases the recombination of photogenerated electron–hole pairs. This was one of the reasons limited the development of WO_3 as a practical photocatalyst. Therefore, one of the principles to improve the photocatalytic performance of WO_3 is to increase the efficiency of electron–hole separation. Loading noble metals on the photocatalyst has been proved as an effectual approach recently [18–20]. Among various noble metals, silver is of considerable interest not only because of the resultant enhanced electron–hole separation but also ascribed to the extension of visible-light absorption and enhanced photocatalytic activity from the surface plasmon resonance (SPR) effect of silver nanoparticles [21,22].

As mentioned above, the microstructures of the photocatalyst also influence the photocatalytic activity significantly. Mesoporous structures exhibit the obvious advantages for the heterogeneous catalysis [23,24]. Especially, ordered mesoporous structures have been proved to be excellent structures for photocatalysis due to their larger surface area and multiple scattering, enable more light to be harvested and also possess continuous pore channels that facilitate the transfer of reactant molecules [25]. Inspired by the above analysis, we conceive that mesoporous silver loaded WO_3 (m-Ag/WO_3) may exhibit high photocatalytic activity. However, the preparation and photocatalytic property of m-Ag/WO_3 have not been reported up to the present.

In the present paper, photocatalytic active m-Ag/WO_3 was synthesized by an ultrasound assisted insertion method. The photooxidation of a common air pollutant acetaldehyde was adopted to

* Corresponding author. Tel.: +86 21 5241 5295; fax: +86 21 5241 3122.
E-mail address: wzwang@mail.sic.ac.cn (W. Wang).

0304-3894/$ – see front matter © 2010 Elsevier B.V. All rights reserved.
doi:10.1016/j.jhazmat.2010.01.098

evaluate the photocatalytic performance of the as-prepared sample under visible-light irradiation. Comparative studies indicate that the photocatalytic activity of m-Ag/WO_3 is much superior to that of pure mesoporous WO_3 (m-WO_3), silver loaded commercial WO_3 (c-Ag/WO_3) and nitrogen-doped TiO_2 (N-TiO_2) nanoparticles under the same conditions. Besides, the photocatalytic mechanism was investigated to understand the much enhanced photocatalytic activity.

2. Experimental

2.1. Sample preparation

Mesoporous silica with cubic Ia3d symmetry (KIT-6) was prepared according to the reference using tri-block copolymer Pluronic P123 (EO20PO70EO20, MW = 5800, Aldrich) as template in an acidic aqueous solution [26].

Mesoporous WO_3 was prepared by a hard template replicating technique. Typically, 1.2 g of 12-phosphotungstic acid (AR, Sinopharm) was dissolved in 10 mL of ethanol, and this solution was incorporated into 0.4 g of as-prepared KIT-6 template under stirring by the impregnation technique. After the ethanol was evaporated gradually, the sample was calcined at 550 °C for 3 h to give a decomposed product of tungsten trioxide inside the silica template. The silica template was removed by 2 M HF solution under stirring. After washing with enough distilled water and drying at room temperature the mesoporous WO_3 sample was obtained.

Silver loaded mesoporous WO_3 was prepared by ultrasound assisted insertion technology. In a typical synthesis, 0.1 g of mesoporous WO_3 was immersed in a bottle filled with a solution of 0.02 g $AgNO_3$ (AR, Sinopharm) in a mixed solution containing 2.5 mL deionized water and 7.5 mL ethanol. The bottle was put in an ultrasonic cleaning bath and connected to a vacuum pump. After sonication under reduced pressure for 10 min, the vacuum pump was turned off and air was allowed to enter the system till normal atmospheric pressure was achieved while the ultrasonic treatment was continued, and the system status was held for another 5 min. Then the suspension was dried in a vacuum oven at 30 °C for 12 h. After that, the powder was put into a sealed reactor filled with methanol vapors and irradiated under a Xe lamp (500 W) for 4 h. This converted the Ag^+ ions into Ag particles.

The N-TiO_2 photocatalyst was prepared by nitrogenization of commercially available TiO_2 powder (surface area 50 $m^2\ g^{-1}$) at 500 °C for 10 h under NH_3 flow [27].

2.2. Characterization

The purity and the crystallinity of the as-prepared samples were characterized by powder X-ray diffraction (XRD) on a Japan Rigaku Rotaflex diffractometer using Cu Kα radiation while the voltage and electric current were held at 40 kV and 100 mA. The transmission electron microscope (TEM) analyses were performed by a JEOL JEM-2100F field emission electron microscope. Energy-dispersive X-ray spectrum (EDS) was collected from an attached Oxford Link ISIS energy-dispersive spectrometer. XPS (X-ray photoelectron spectroscopy) measurement was carried out in a VG-Microtech Multilab electron spectrometer using Mg Kα (1253.6 eV) radiation source. The N_2-sorption measurement was performed using Micromeritics Tristar 3000 at 77 K, and specific surface area and the pore size distribution were calculated using the Brunauer–Emmett–Teller (BET) and Barrett–Joyner–Halenda (BJH) methods, respectively. UV–vis diffuse reflectance spectrum (DRS) of the sample was measured by using a Hitachi U-3010 UV–vis spectrophotometer.

2.3. Photocatalytic test

The photocatalytic activity of the samples was evaluated by the degradation of acetaldehyde under visible-light irradiation of a 500 W Xe lamp with a 420 nm cutoff filter. Typically, 0.2 g of photocatalyst was placed at the bottom of a gas-closed reactor at room temperature (capacity 600 mL). This reactor was made of glass and had a quartz window. The reaction gas mixture (1 atm) consisted of 100 ppm CH_3CHO and N_2 balance gas. Prior to commencing irradiation, the reaction system was equilibrated for about 120 min until no changes in the concentrations of acetaldehyde and CO_2 were monitored. Gaseous samples (1 mL) were periodically extracted and analyzed by a gas chromatography (GC) equipped with a flame ionization detector (N_2 carrier) and the catalytic conversion furnace.

3. Results and discussion

3.1. Structural characteristics

The crystalline phase and mesostructural ordering of the m-WO_3 and m-Ag/WO_3 samples were characterized by both wide-angle X-ray diffraction (WXRD) and low-angle X-ray diffraction (LXRD) measurements. As shown in Fig. 1a, WXRD demonstrates the m-WO_3 sample was well crystallized in a single phase and all of the diffraction peaks can be indexed to monoclinic WO_3 (JCPDS

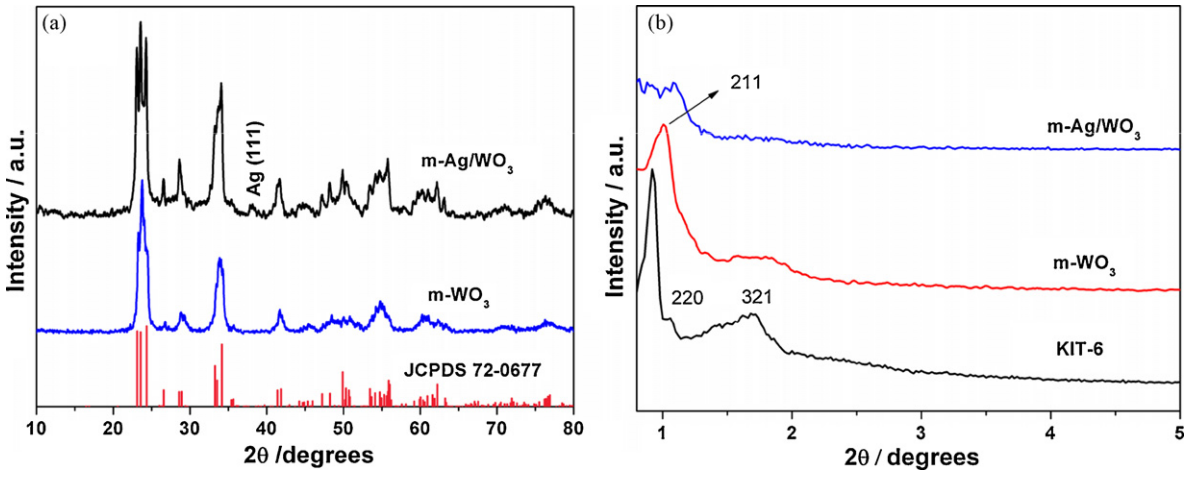

Fig. 1. (a) Wide-angle XRD pattern of the as-prepared m-WO_3 and m-Ag/WO_3 samples and (b) small-angle XRD patterns of mesoporous cubic KIT-6 silica, m-WO_3 and m-Ag/WO_3 samples.

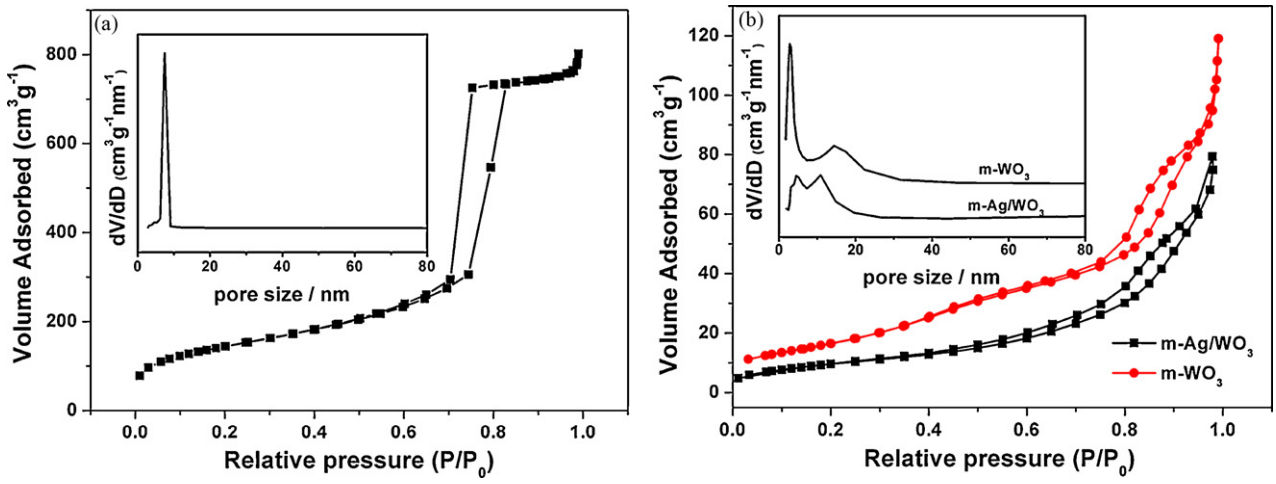

Fig. 2. (a) N_2-sorption isotherm and corresponding pore size distribution curves (inset) for replicate template KIT-6 and (b) N_2-sorption isotherms for as-prepared m-WO_3 and m-Ag/WO_3 samples and corresponding pore size distribution curve (inset).

72-0677). The WXRD of the m-Ag/WO_3 sample was similar to that of m-WO_3 except for the diffraction peak of Ag (1 1 1) at 2θ of 38.1° which is attributed to cubic Ag (JCPDS 04-0783). The crystal size of m-WO_3 sample was about 8.9 nm based on the Scherrer formula. By the same method, the crystal size of WO_3 and Ag in the m-Ag/WO_3 sample was estimated to be 8.7 and 9.1 nm respectively. According to the LXRD in Fig. 1b, template KIT-6 exhibits three well-resolved diffraction peaks in the 2θ range between 0.5° and 3°, which can be indexed as (2 1 1), (2 2 0) and (3 2 1) reflections associated with cubic symmetry (*Ia*3*d* space group). The m-WO_3 sample shows the similar characteristic low angle diffraction peaks as the silica template with slightly shifted peak position to higher angle, suggesting that the WO_3 product retains the ordered mesoporous structure and inherits the cubic Ia3d symmetry structure of the template.

The nitrogen adsorption/desorption isotherms of the samples have been recorded and shown in Fig. 2. The isotherm for KIT-6 was of type IV classification (Fig. 2a). Both of the as-prepared m-WO_3 and m-Ag/WO_3 samples show similar isotherm curves to that of the KIT-6 template, with a weak jump at $P/P_0 = 0.3–0.5$ and another jump at $P/P_0 = 0.8–0.9$ (Fig. 2b), which is the characteristic of mesoporous solids. This indicates that the mesostructures of m-Ag/WO_3 sample have been kept after the incorporation of metallic Ag particles. The data of the specific surface areas of these samples with the corresponding pore sizes and pore volumes are summarized in Table 1. The KIT-6 template had a surface area of 522 $m^2\ g^{-1}$, a pore volume of 1.17 $cm^3\ g^{-1}$, and a pore size of 7.7 nm, while the m-WO_3 sample had a much smaller surface area and a pore volume of 60 $m^2\ g^{-1}$ and 0.14 $cm^3\ g^{-1}$, respectively. The BET specific surface area and the pore volume of m-Ag/WO_3 composite were further decreased compared with that of the m-WO_3 sample. This is due to the fact that Ag nanoparticles were dispersed within the pore channels of the mesoporous WO_3 support, leading to the blocking of the pore channels. The wall thickness of the as-prepared materials was calculated by using the relation $b = [1 - V_p\rho/(1 + V_p\rho)]a_0/3.0919$, where ρ is the density and V_p is the pore volume [28]. The calculated wall thicknesses of KIT-6 and m-WO_3 were 3.5 and 6.13 nm, respectively. The calculated pore wall of KIT-6 was very similar to the pore size of m-WO_3 centered at 3.1 nm (inset of Fig. 2b). Some large mesopores with an average pore size of 14 nm in the m-WO_3 sample (inset of Fig. 2b) was attributable to the wall junctions in KIT-6 [29].

Typical TEM images of the m-WO_3 sample are shown in Fig. 3, which reveals clearly the aligned nanorods and mesoporous structure of the as-prepared m-WO_3. The crystal size of WO_3 was estimated to be around 8 nm and is close to the pore size (7.7 nm) of the hard template KIT-6, indicating that the m-WO_3 product is a good replica of the mesoporous structure of silica template. Besides, the result of crystal size was in good agreement with the estimated value obtained using the Scherrer equation based on the XRD patterns (8.9 nm) and higher than the 6.13 nm calculated from the BET result. The difference between these two values for the pore wall thickness may be due to an error inherent in the calculation method based on the BET result.

TEM images of m-Ag/WO_3 sample in Fig. 4a–c show that Ag nanoparticles are well dispersed in the pore structure of mesoporous WO_3. The inset SAED pattern in Fig. 4a was recorded on the marked area, which reveals the coexistence of crystalline Ag and WO_3 in the m-Ag/WO_3 sample. An enlarged TEM image in Fig. 4b shows the pore channels of the silver loaded sample were impregnate compared with that of bare WO_3 as a result of the dispersed Ag nanoparticles in the pore channels. A high-resolution TEM image in Fig. 4c shows two kinds of crystal lattice stripes. The smaller one of $d = 0.24$ nm belongs to the metallic silver (JCPDS 04-0783) and another one of $d = 0.37$ nm belongs to WO_3 (JCPDS 72-0677), which is an additional evidence proving the Ag particles existed in the pores of the support. A more direct evidence of Ag nanoparticles dispersed in the WO_3 matrix is that clear Ag signals could be easily detected by EDS obtained on the m-Ag/WO_3 composites (Fig. 4d). A quantitative study of the EDS results gives the weight ratio of Ag in the composite is 9.17%.

The oxidation state of the Ag species is examined by XPS in the Ag 3d5/2 and Ag 3d3/2 binding energy regions, as shown in Fig. 5.

Table 1
Pore structure parameters of KIT-6, m-WO_3 and m-Ag/WO_3 samples.

Sample	XRD results (nm)	S_{BET} (m^2/g)	Pore volume (cm^3/g)	BJH pore size (nm)	Lattice parameter, *a* (nm)[a]
KIT-6	$d_{211} = 9.625$	522	1.17	7.7	23.5
m-WO_3	$d_{211} = 8.850$	60	0.14	8.4	21.6
m-Ag/WO_3		36	0.10		

[a] $a = d_{hkl}(h^2 + k^2 + l^2)^{1/2}$ is a cubic lattice parameter calculated from X-ray data.

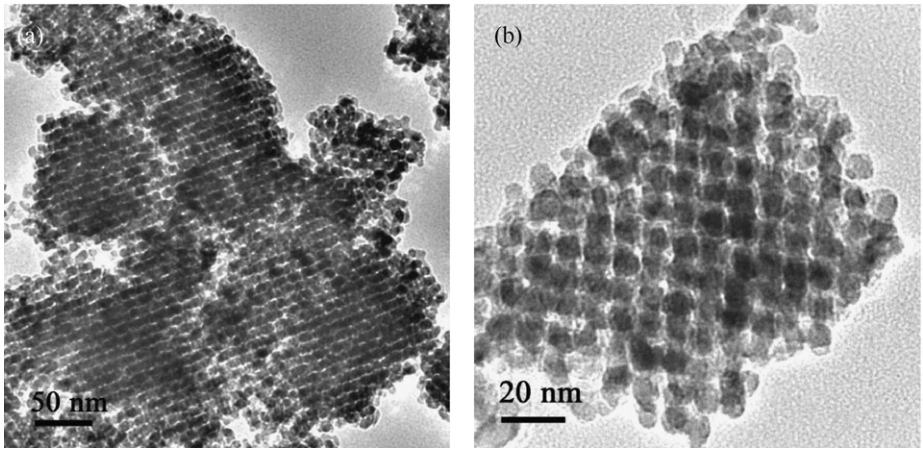

Fig. 3. TEM images of as-prepared m-WO_3 sample.

The Ag 3d5/2 peak is centered at 368.5 eV whereas the Ag 3d3/2 peak is found at 374.5 eV, with a spin energy separation of 6.0 eV. This is characteristic of metallic silver [30].

The optical absorption of the as-prepared m-WO_3 and m-Ag/WO_3 samples was measured by using an UV–vis spectrometer. As shown in Fig. 6, both of the samples have a photoabsorption from UV light to visible light and the wavelength of the absorption-edge of the m-WO_3 is at 482 nm. The optical band gap of the as-prepared m-WO_3 sample was estimated from the absorption data by the following equation near the band edge: $\alpha h\nu = A(h\nu - E_g)^{n/2}$ [31], where α, ν, E_g and A are absorption coefficient, light frequency, band gap and a constant, respectively. The value of n is 1 or 4 for a direct

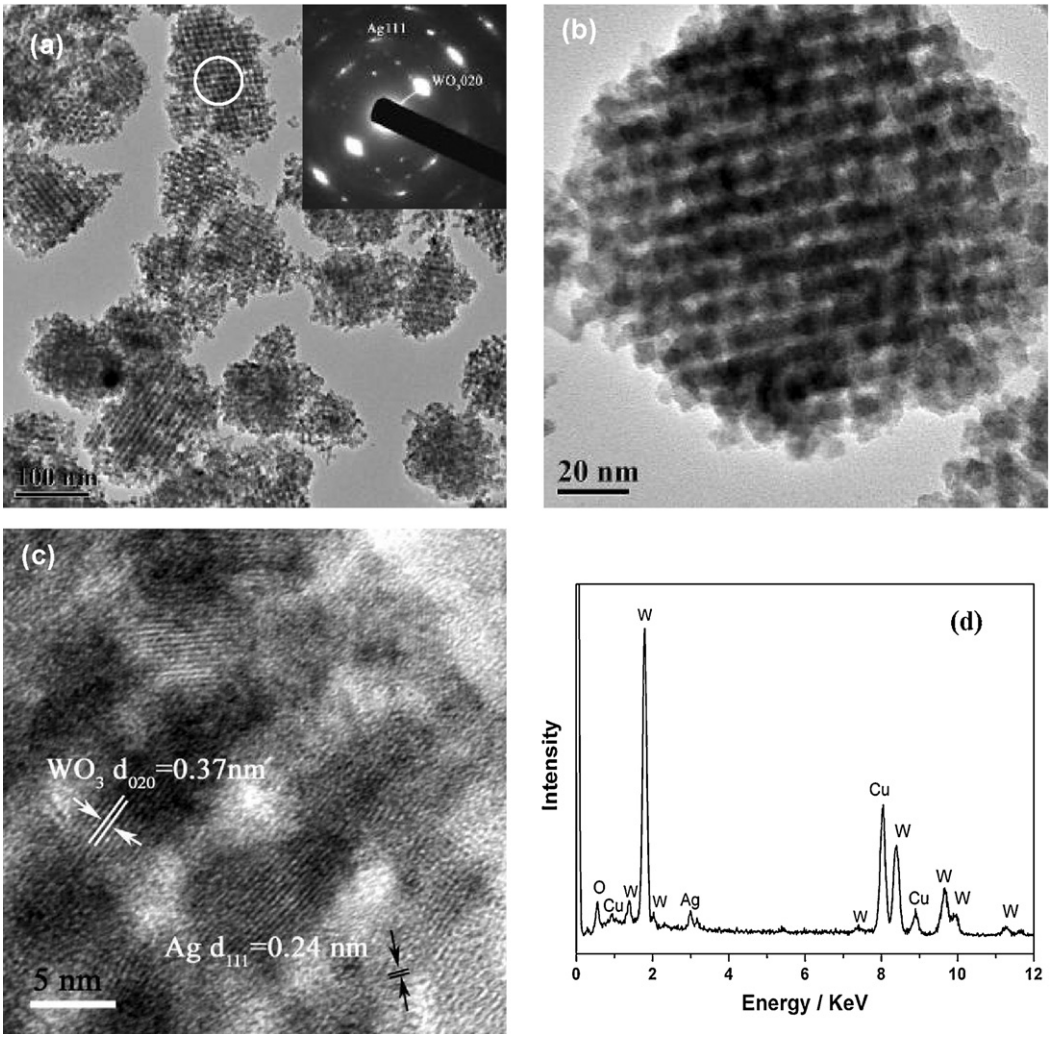

Fig. 4. TEM image (a and b) and HRTEM image (c) of the as-prepared m-Ag/WO_3 sample and (d) EDS spectrum of the as-prepared m-Ag/WO_3 sample. Inset of (a): SAED pattern recorded at the marked area of (a).

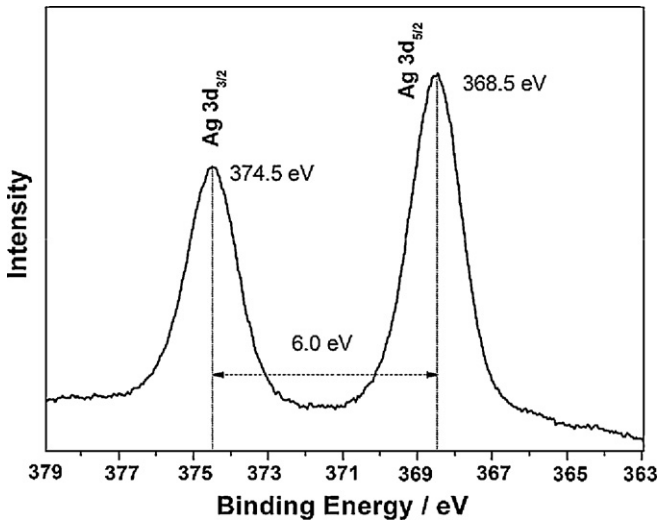

Fig. 5. XPS spectra of the as-prepared m-Ag/WO_3 sample in the Ag 3d5/2 and Ag 3d3/2 binding energy region.

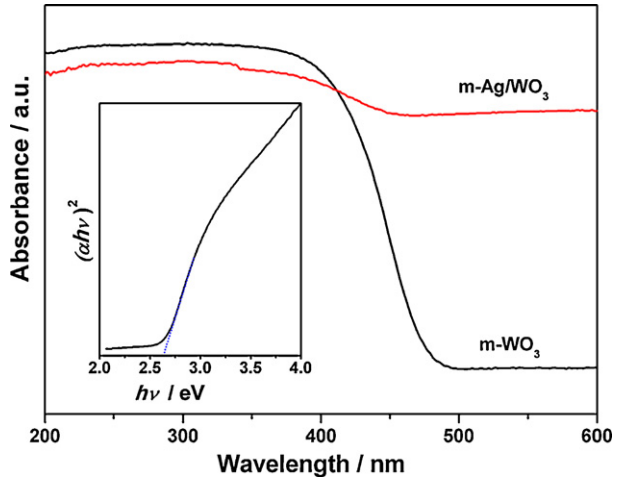

Fig. 6. Typical diffuse reflection spectra of the as-prepared m-WO_3 and m-Ag/WO_3 samples. The inset is the $ah\nu$–$h\nu$ curve.

or indirect transition respectively. When an proximate value of E_g was used and the line of $\ln(ah\nu)$ vs $\ln(h\nu - E_g)$ was plotted, the value of n was determined to be 1 indicating a direct optical transition which is similar to the previous report on monoclinic WO_3 [32,33]. The energy of the band gap of m-WO_3 can thus be obtained from the plots of $(\alpha h\nu)^2$ versus photon energy $h\nu$, as shown in the inset of Fig. 6. The value estimated from the intercept of the tangent to the plot is 2.64 eV. Fig. 6 also indicates that loading silver on the m-WO_3 sample enhanced the visible-light absorption.

3.2. photocatalytic activity

The photocatalytic activities of m-Ag/WO_3 and other photocatalysts were evaluated by the photodegradation of a common air pollutant of acetaldehyde under visible-light irradiation. The photocatalytic activity was examined by measuring the production of CO_2. Fig. 7a shows typical plots of the increase in CO_2 concentration as a function of irradiation time on different photocatalysts. As shown in Fig. 7a, with the as-prepared m-Ag/WO_3 sample as photocatalyst, the CO_2 concentration was dramatically increased at initial 20 min and about 90% of acetaldehyde was oxidized into CO_2 after 60 min, showing the excellent photocatalytic activity under visible-light irradiation. For comparison, the photocatalytic activities of m-WO_3, c-Ag/WO_3 and N-TiO_2 samples were also tested. After being irradiated under visible light for 60 min, the degradation of acetaldehyde by c-Ag/WO_3 was 17% only, which is the lowest among these photocatalysts. Under the same conditions, the degradation of acetaldehyde by m-WO_3 and N-TiO_2 were 53% and 30% respectively, which is also less efficient than that of m-Ag/WO_3 sample. To enable a quantitative comparison, the decomposition rates within the first 20 min were proposed to represent the photocatalytic activities because this region is most likely to be dominated by pure light-intensity-limited conditions [34]. At the initial 20 min, the decomposition of acetaldehyde by m-Ag/WO_3, m-WO_3, c-Ag/WO_3 and N-TiO_2 samples were 51%, 18%, 6% and 8% respectively. Then the photocatalytic activity of m-Ag/WO_3 is about three and six times higher than that of m-WO_3 and N-TiO_2 respectively, indicating an obvious advantage of the m-Ag/WO_3 sample under visible-light irradiation. To investigate the recyclability of the m-Ag/WO_3 photocatalyst for the degradation of acetaldehyde, sample powders after photocatalytic reactions were collected for the subsequent photoreaction cycle. As shown in Fig. 7b, the photocatalytic activity of m-Ag/WO_3 on acetaldehyde degradation was well-maintained.

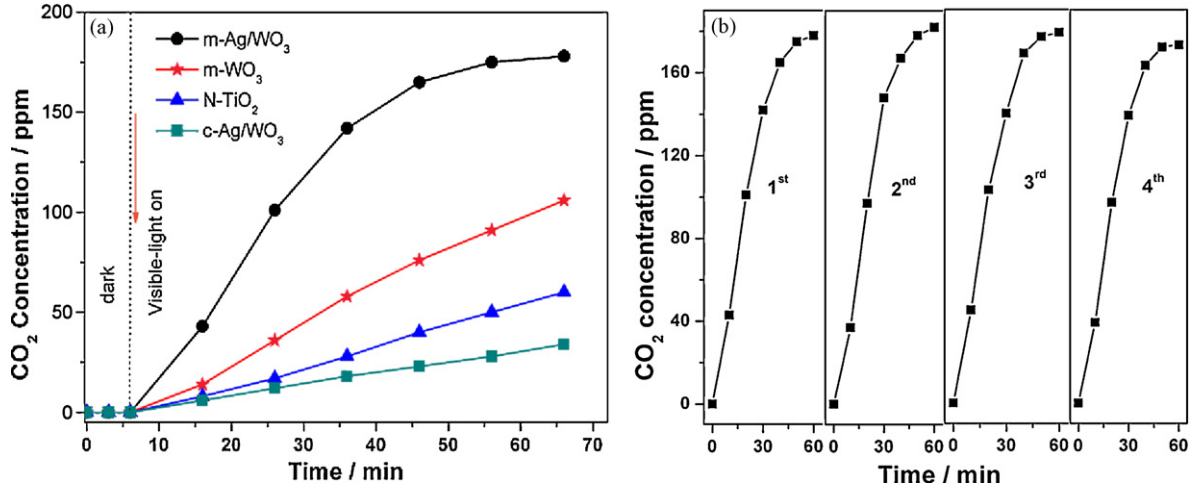

Fig. 7. (a) Increase in CO_2 concentration as a function of irradiation time during the photocatalytic degradation of acetaldehyde by different photocatalysts and (b) recyclability of m-Ag/WO_3 sample in photodegradation of acetaldehyde.

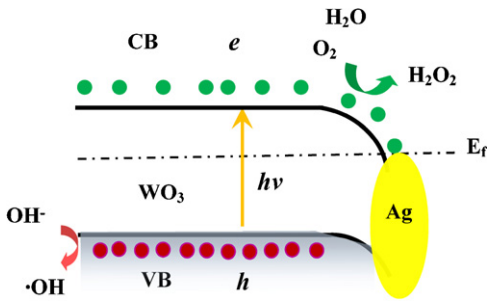

Fig. 8. Schematic illustration of the photocatalytic mechanism of the m-Ag/WO_3 sample.

These results strongly suggested that loading silver nanoparticles greatly enhanced the photocatalytic performance. Investigations on the photocatalytic mechanism are necessary to understand this enhanced photocatalytic activity. Here we discuss it in detail based on the band structure of the Ag–WO_3 heterojunction. The work function of WO_3 (5.7 eV) is larger than that of Ag (4.7 eV) [35]. If the Ag contacts WO_3, the electrons will migrate from silver to the conduction band (CB) of WO_3 to achieve the Fermi level equilibration. As a result, the surface of the WO_3 accumulates excess electrons, while the Ag exhibits an excess positive charge, and the deflexed energy band forms at the Ag–WO_3 interface. When the WO_3 catalysts are illuminated under visible light, electrons (e^-) in the valence band (VB) of WO_3 can be excited to the CB and simultaneously the same amount of holes (h^+) were generated in the VB. The scheme for the photocatalytic process is shown in Fig. 8. In the m-Ag/WO_3 system, the deflexed energy band in the space charge region facilitates the rapid transfer of the as-excited electrons from WO_3 to Ag nanoparticles, which decreases the recombination of the photogenerated electron–hole pairs. As the WO_3 has a low CB level (+0.5 V vs NHE) which is more positive than the potential for the single-electron reduction of oxygen [20], electrons accumulated at Ag particles or the conduction band of WO_3 may be transferred to surface-adsorbed oxygen molecules to form H_2O_2 by multi-electron reduction of O_2. The photoinduced holes with high oxidation potential (+3 V vs NHE) [36] are apt to react with surface-bound H_2O or OH^- to produce the hydroxyl radical species $^{\bullet}OH$ which is an extremely strong oxidant for the mineralization of organic contaminants. Based on the above analysis, the photocatalytic reaction can be expressed as follows:

$$WO_3 + h\nu \rightarrow e^- + h^+ \quad (1)$$

$$h^+ + OH^- \rightarrow {}^{\bullet}OH \quad (2)$$

$$h^+ + H_2O \rightarrow {}^{\bullet}OH + H^+ \quad (3)$$

$$e^- + Ag^+ \rightarrow Ag \quad (4)$$

$$2e^- + O_2 + 2H_2O \rightarrow H_2O_2 + 2OH^- \quad (5)$$

$$\text{Acetaldehyde} + {}^{\bullet}OH(\text{or}h^+) \rightarrow CO_2 \quad (6)$$

4. Conclusion

Mesoporous silver loaded WO_3 has been successfully synthesized by an ultrasound assisted insertion method. The as-prepared m-Ag/WO_3 sample exhibits excellent photocatalytic decomposition of a common air pollutant of acetaldehyde under visible-light irradiation. Comparative studies indicated that the photocatalytic activity of the m-Ag/WO_3 sample is much superior to that of m-WO_3, c-Ag/WO_3 and N-TiO_2 under the same conditions. The photocatalytic mechanism was investigated to understand the much enhanced photocatalytic activity, which is mainly attributed to the largely improved charge separation of the photogenerated electrons and holes in the Ag–WO_3 heterojunction, allowing both of the electrons and holes participating in the overall photocatalytic reaction.

Acknowledgements

This work is financially supported by the National Natural Science Foundation of China (Nos. 50732004 and 50672117) National Basic Research Program of China (973 Program, 2007CB613305) and Nanotechnology Programs of Science and Technology Commission of Shanghai Municipality (0852nm00500).

References

[1] W. Zhao, W.H. Ma, C.C. Chen, J.C. Zhao, Z.G. Shuai, Efficient degradation of toxic organic pollutants with $Ni_2O_3/TiO_{2-x}B_x$ under visible irradiation, J. Am. Chem. Soc. 126 (2004) 4782–4783.
[2] X. Hu, C. Hu, J. Qu, Photocatalytic decomposition of acetaldehyde and *Escherichia coli* using NiO/$SrBi_2O_4$ under visible light irradiation, Appl. Catal. B: Environ. 69 (2006) 17–23.
[3] M.M. Uddin, M.A. Hasnat, A.J. Samed, R.K. Majumdar, Influence of TiO_2 and ZnO photocatalysts on adsorption and degradation behaviour of Erythrosine, Dyes Pigments 75 (2007) 207–212.
[4] A. Petrozza, C. Groves, H.J. Snaith, Electron transport and recombination in dye-sensitized mesoporous TiO_2 probed by photoinduced charge-conductivity modulation spectroscopy with monte carlo modeling, J. Am. Chem. Soc. 130 (2008) 12912–12920.
[5] M. Sleiman, P. Conchon, C. Ferronato, J.-M. Chovelon, Photocatalytic oxidation of toluene at indoor air levels (ppbv): towards a better assessment of conversion, reaction intermediates and mineralization, Appl. Catal. B: Environ. 86 (2009) 159–165.
[6] W. Choi, A. Termin, M.R. Hoffmann, The role of metal ion dopants in quantum-sized TiO_2: correlation between photoreactivity and charge carrier recombination dynamics, J. Phys. Chem. 98 (1994) 13669–13679.
[7] R. Asahi, T. Morikawa, T. Ohwaki, K. Aoki, Y. Taga, Visible-light photocatalysis in nitrogen-doped titanium oxides, Science 293 (2001) 269–271.
[8] S.U.M. Khan, M. Al-Shahry, J.W.B. Ingler, Efficient photochemical water splitting by a chemically modified n-TiO_2, Science 297 (2002) 2243–2245.
[9] S. Sakthivel, H. Kisch, Daylight photocatalysis by carbon-modified titanium dioxide, Angew. Chem. Int. Ed. 42 (2003) 4908–4911.
[10] L. Zhang, I. Djerdj, M. Cao, M. Antonietti, M. Niederberger, Nonaqueous sol–gel synthesis of a nanocrystalline $InNbO_4$ visible-light photocatalyst, Adv. Mater. 19 (2007) 2083–2086.
[11] Y. Guo, X. Quan, N. Lu, H. Zhao, S. Chen, High photocatalytic capability of self-assembled nanoporous WO_3 with preferential orientation of (002) planes, Environ. Sci. Technol. 41 (2007) 4422–4427.
[12] Z.-G. Zhao, M. Miyauchi, Nanoporous-walled tungsten oxide nanotubes as highly active visible-light-driven photocatalysts, Angew. Chem. Int. Ed. 47 (2008) 7051–7055.
[13] J. Yu, L. Qi, B. Cheng, X. Zhao, Effect of calcination temperatures on microstructures and photocatalytic activity of tungsten trioxide hollow microspheres, J. Hazard. Mater. 160 (2008) 621–628.
[14] G.R. Bamwenda, H. Arakawa, The visible light induced photocatalytic activity of tungsten trioxide powders, Appl. Catal. A 210 (2001) 181–191.
[15] J.R. Darwent, A. Mills, Photo-oxidation of water sensitized by WO_3 powder, J. Chem. Soc., Faraday Trans. 78 (1982) 359–367.
[16] W. Erbs, J. Desilvestro, E. Borgarello, M. Gratzel, Visible-light-induced O_2 generation from aqueous dispersions of WO_3, J. Phys. Chem. 88 (1984) 4001–4006.
[17] R. Abe, K. Sayama, H. Sugihara, Development of new photocatalytic water splitting into H_2 and O_2 using two different semiconductor photocatalysts and a shuttle redox mediator IO_3^-/I^-, J. Phys. Chem. B 109 (2005) 16052–16061.
[18] H. Li, Z. Bian, J. Zhu, Y. Huo, H. Li, Y. Lu, Mesoporous Au/TiO_2 nanocomposites with enhanced photocatalytic activity, J. Am. Chem. Soc. 129 (2007) 4538–4539.
[19] J. Yu, J. Xiong, B. Cheng, S. Liu, Fabrication and characterization of Ag–TiO_2 multiphase nanocomposite thin films with enhanced photocatalytic activity, Appl. Catal. B: Environ. 60 (2005) 211–221.
[20] R. Abe, H. Takami, N. Murakami, B. Ohtani, Pristine simple oxides as visible light driven photocatalysts: highly efficient decomposition of organic compounds over platinum-loaded tungsten oxide, J. Am. Chem. Soc. 130 (2008) 7780–7781.
[21] H. Zhang, G. Wang, D. Chen, X. Lv, J. Li, Tuning photoelectrochemical performances of Ag-TiO_2 nanocomposites via reduction/oxidation of Ag, Chem. Mater. 20 (2008) 6543–6549.
[22] K. Awazu, M. Fujimaki, C. Rockstuhl, J. Tominaga, H. Murakami, Y. Ohki, N. Yoshida, T. Watanabe, A plasmonic photocatalyst consisting of silver nanoparticles embedded in titanium dioxide, J. Am. Chem. Soc. 130 (2008) 1676–1680.
[23] A.Q. Wang, C.M. Chang, C.Y. Mou, Evolution of catalytic activity of Au–Ag bimetallic nanoparticles on mesoporous support for CO oxidation, J. Phys. Chem. B 109 (2005) 18860–18867.
[24] B. Chowdhitry, J.J. Bravo-Suarez, M. Date, S. Tsubota, M. Haruta, Trimethylamine as a gas-phase promoter: highly efficient epoxidation of propylene over supported gold catalysts, Angew. Chem., Int. Ed. 45 (2006) 412–415.

[25] J.C. Yu, X.C. Wang, X.Z. Fu, Pore-wall chemistry and photocatalytic activity of mesoporous titania molecular sieve films, Chem. Mater. 16 (2004) 1523–1530.
[26] F. Kleitz, S.H. Choi, R. Ryoo, Cubic Ia3d large mesoporous silica: synthesis and replication to platinum nanowires, carbon nanorods and carbon nanotubes, Chem. Commun. 17 (2003) 2136–2137.
[27] K. Maeda, Y. Shimodaira, B. Lee, K. Teramura, D. Lu, H. Kobayashi, K. Domen, Studies on $TiN_xO_yF_z$ as a visible-light-responsive photocatalyst, J. Phys. Chem. C 111 (2007) 18264–18270.
[28] P.I. Ravikovitch, A.V. Neimark, Relations between structural parameters and adsorption characterization of templated nanoporous materials with cubic symmetry, Langmuir 16 (2000) 2419–2423.
[29] K. Jiao, B. Zhang, B. Yue, Y. Ren, S.X. Liu, S.R. Yan, C. Dickinson, W.Z. Zhou, H.Y. He, Growth of porous single-crystal Cr_2O_3 in a 3-D mesopore system, Chem. Commun. 45 (2005) 5618–5620.
[30] J.F. Moulder, W.F. Stickle, P.E. Sobol, K.D. Bomben, in: J. Chastain (Ed.), Handbook of X-ray Photoelectron Spectroscopy, Perkin-Elmer Corporation, USA, 1992.
[31] M.A. Butler, Photoelectrolysis and physical properties of the semiconducting electrode WO_3, J. Appl. Phys. 48 (1977) 1914–1920.
[32] A.P. Finlayson, V.N. Tsaneva, L. Lyons, M. Clark, B.A. Glowacki, Evaluation of Bi–W-oxides for visible light photocatalysis, Phys. Stat. Sol. (a) 203 (2006) 327–335.
[33] P.S. Patil, S.H. Mujawar, A.I. Inamdar, P.S. Shinde, H.P. Deshmukh, S.B. Sadale, Structural, electrical and optical properties of TiO_2 doped WO_3 thin films, Appl. Surf. Sci. 252 (2005) 1643–1650.
[34] Y. Ohko, A. Fujishima, K. Hashimoto, Autooxidation of acetaldehyde initiated by TiO_2 photocatalysis under weak UV illumination, J. Phys. Chem. B 102 (1998) 2699–2704.
[35] Gy. Vida, V.K. Josepovits, M. Gyõr, P. Deák, Characterization of tungsten surfaces by simultaneous work function and secondary electron emission measurements, Microsc. Microanal. 9 (2003) 337–342.
[36] T. Arai, M. Yanagida, Y. Konishi, Y. Iwasaki, H. Sugihara, K. Sayama, Efficient complete oxidation of acetaldehyde into CO_2 over $CuBi_2O_4/WO_3$ composite photocatalyst under visible and UV light irradiation, J. Phys. Chem. C 111 (2007) 7574–7577.